Theory of emission from an active photonic lattice

Weng W. Chow
Sandia National Laboratories, Albuquerque, New Mexico 87185-0601, USA
(Received 30 March 2005; revised manuscript received 18 July 2005; published 27 January 2006)

The emission from a radiating source embedded in a photonic lattice is calculated. The analysis considers the photonic lattice and free space as a combined system. Furthermore, the radiating source and electromagnetic field are quantized. Results show the deviation of the photonic lattice spectrum from the blackbody distribution, with intracavity emission suppressed at certain frequencies and enhanced at others. In the presence of rapid population relaxation, where the photonic lattice and blackbody populations are described by the same equilibrium distribution, it is found that the enhancement does not result in output intensity exceeding that of the blackbody at the same frequency. However, for slow population relaxation, the photonic lattice population has a greater tendency to deviate from thermal equilibrium, resulting in output intensities exceeding those of the blackbody, even for identically pumped structures.

DOI: 10.1103/PhysRevA.73.013821 PACS number(s): 42.50.Ct, 42.50.Nn, 44.40.+a, 42.70.Qs

I. INTRODUCTION

One of the many novel optical phenomena exhibited by photonic lattices is the modification of spontaneous emission properties [1,2]. A photonic lattice can funnel radiation into narrow energy bands, where exceedingly high intensities at photonic lattice band edges have been predicted theoretically and observed experimentally [3–6]. A question is whether the peak intensities exceed those of a blackbody under similar experimental conditions [7–12]. The answer is important for scientific understanding and can impact the development of new light sources.

It is generally agreed that a higher photonic-lattice density of states will increase the intracavity intensity. The debate concerns the output intensity in comparison with that of a blackbody. Arriving at an answer is difficult experimentally because it is difficult to ensure that the comparison is made under similar conditions. Theoretically, the difficulty lies with the treatment of the matter and optical aspects of the problem [13]. The derivation of the matter equations requires knowledge of the normal modes of the optical structure, preferably in the form of an orthonormal basis. However, such a basis set is not rigorously defined for a finite photonic lattice with outcoupling loss. This problem occurs also in laser theory, where one usually begins with the Fox-Li modes for a Fabry-Perot cavity with perfectly reflecting mirrors and introduces a loss mechanism to represent the outcoupling [14]. Such a phenomenological approach is inadequate for the present problem because of the inconsistency arising from separating the treatments of the eigenmode problem and the outcoupling effects.

The approach taken in this paper considers the photonic lattice and free space outside of the photonic lattice as one combined system (see Fig. 1). We follow the method of an earlier paper on the linewidth of a Fabry-Periot laser [15] in representing free space by a very large cavity. The photonic lattice is approximated by a series of semitransparent interfaces. We begin with discussing the one-dimensional geometry [7,16], which we will show to contain the essential features necessary for addressing our question. Section II discusses the equations and boundary conditions obeyed by the modes of our "universe." The determination of the eigenfrequencies and eigenfunctions requires the simultaneous diagonalization of a usually large matrix and the solution of a transcendental equation. A numerical procedure for a photonic lattice of arbitrary size and interface transmission is presented in the Appendix.

In Sec. III, the radiation field is expanded in term of these large number of modes and quantized. The radiation source is also treated quantum mechanically, as an inhomogeneously broadened ensemble of two-level atoms confined within the photonic lattice structure. The equations of motion for the photon number and atomic populations are derived in this section. We choose a fully quantized (i.e., quantized matter and field) treatment based on Einstein's derivation of the Planck radiation law, which showed the importance of a consistent treatment of stimulated and spontaneous emission processes [17]. Einstein was able to circumvent a fully quantized theory by using the Wien displacement law, which applied only to emission in free space. For the photonic lattice, such a general relation does not exist.

There are several recent calculations of photonic-lattice emission where the emitting source is a classically described current [12,16]. An advantage of our treatment over these classical ones is that by paralleling the Planck radiation law derivation, our comparison of photonic-lattice and blackbody emission spectra is appreciably more straightforward. Moreover, the fluctuation-dissipation theorem [18], which is an essential assumption in classical calculations [12,16], appears as a result in a fully quantized treatment because spontaneous emission is treated from first principles.

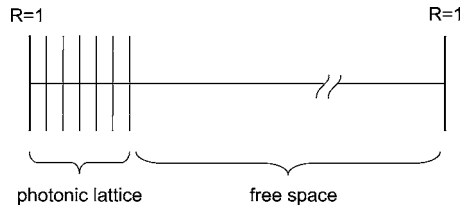

FIG. 1. Model of a photonic lattice connected to a large cavity approximating the universe.

Section IV describes a spectrometer model used to determine the emission spectrum. Section V uses the theory developed in the earlier sections to investigate emission from an active photonic lattice that is excited by an external pump and allowed to equilibrate with a thermal bath via collisions. The radiation field spectra measured inside and outside the photonic lattice are described. Comparison of photonic lattice and blackbody emissions is discussed for equilibrium and nonequilibrium situations.

Section VI summarizes the extension to a three-dimensional (3D) geometry. The comparison between photonic-lattice and blackbody spectra is made assuming a spherically symmetric photonic-lattice dielectric function. The 3D treatment is important for three reasons. First, it proves that the theory can retrieve Planck's blackbody distribution in the absence of a photonic lattice. Second, it verifies the 1D treatment in terms of containing the necessary physics for answering the question of photonic-lattice versus blackbody thermal emission. Last, it points out the substantial increase in numerical demands with increase dimensionality, thus justifying our concentration on the 1D analysis to facilitate physical understanding and tractability of numerics.

II. MODES OF THE COMBINED PHOTONIC-LATTICE AND FREE-SPACE SYSTEM

In this section, the eigenmodes for a photonic lattice coupled to the outside world are derived using the model depicted in Fig. 1. The universe, which embeds the photonic lattice, is represented by a very large cavity with perfectly reflecting walls at $z=0$ and $z=L$. (End results are extrapolated by taking the limit $L\to\infty$.) The photonic lattice is modeled as a series of coupled resonators with semitransparent interfaces. Following Spencer and Lamb [19], the semitransparent interfaces are described as very thin surfaces with very large dielectric constants. As an idealization, we use dielectric "bumps," giving a dielectric permittivity

$$\epsilon(z)=\epsilon_0\left[1+\frac{\eta}{\bar{k}}\sum_{j=1}^{N_{pl}}\delta(z-z_j)\right], \tag{1}$$

where $\eta=2\sqrt{(1-T_{pl})/T_{pl}}$, T_{pl} is an effective transmission at each interface located at z_j, $\bar{k}$ is the average magnitude of the electromagnetic field wave vector, and N_{pl} is the number of periods making up the photonic lattice. For brevity, we assume the background permittivity inside the photonic lattice to be that of vacuum ϵ_0.

Using the above dielectric function in Maxwell equations gives the following differential equation for the eigenmodes of the combined photonic-lattice and free-space system:

$$\frac{d^2}{dz^2}u_k(z)=-\mu_0\epsilon(z)\Omega_k^2u_k(z), \tag{2}$$

where μ_0 is the permeability in vacuum, Ω_k is the eigenfrequency, and k labels the eigenmode. The boundary conditions are obtained by first noting that the system is bounded by totally reflecting surfaces, so that

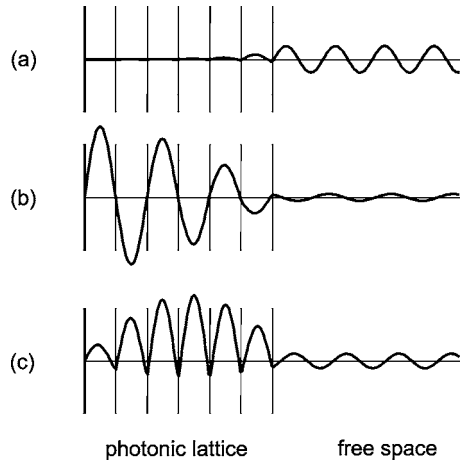

FIG. 2. Eigenfunctions of a six-period photonic lattice coupled to free space for interface transmission $T_{pl}=0.10$. The figure shows nonresonant (a) and resonant (b), (c) photonic-lattice modes.

$$u_k(0)=u_k(L)=0. \tag{3}$$

Integrating Maxwell's equations across the bump gives the boundary conditions

$$u_k(z_j^+)=u_k(z_j^-), \tag{4}$$

$$\frac{d}{dz}u_k(z_j^+)-\frac{d}{dz}u_k(z_j^-)=-\eta k u_k(z_j), \tag{5}$$

where the superscripts − and + indicate the positions immediately before and after an interface, respectively. Integrating by parts (2) gives the orthogonality relation

$$\int_0^L dz\epsilon(z)u_k(z)u_l(z)=\epsilon_0\delta_{k,l}. \tag{6}$$

Plotted in Fig. 2 are examples of eigenfunctions for a six-period ($N_{pl}=6$) photonic lattice with effective interface transmission $T_{pl}=0.1$. Most of the solutions are not resonant with the photonic lattice, so that mode amplitude is negligible inside the photonic lattice, as shown in Fig. 2(a). Figures 2(b) and 2(c) show examples of photonic-lattice modes, where the latter figure clearly depicts the first derivative discontinuities at the interfaces.

We show in Figs. 3 and 4 that the model can reproduce the photonic-lattice properties relevant to our study. Figure 3 illustrates the formation of bands and band gaps, by plotting the frequencies of the photonic-lattice modes [i.e., modes depicted Figs. 2(b) and 2(c)] versus the interface transmission. Not plotted are the large number of free-space modes [Fig. 2(a)], with mode separation $\Omega=\pi c/L\to 0$ as the system length $L\to\infty$. At $T_{pl}=0$, the photonic-lattice modes are simply the modes of six uncoupled resonators, each of length a; i.e., they are N_{pl}-fold degenerate and have frequencies $\Omega=m\pi c/a$ where m is an integer. The degeneracy is removed with coupling among sections of the photonic lattice. The result is groupings of states separated by energy gaps, as shown in the figure. As N_{pl} become very large, the groups of states become continuous bands, with the photonic-lattice

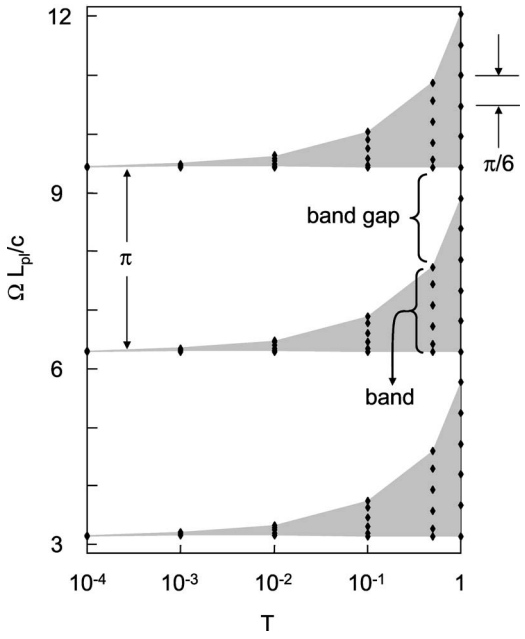

FIG. 3. Eigenfrequency versus interface transmission for a six-period photonic lattice. The points indicate the actual eigenmodes of the finite structure, while the shaded regions illustrate the extent of the bands of photonic-lattice states when the number of periods become very large.

modes residing entirely within the shaded regions and the free-space modes residing outside. At $T_{pl}=1$, the model (with a very long L) approximates the free-space situation.

Figure 4 shows that the model can also reproduce the significant flattening of the photonic-lattice dispersion at the bandedges. Plotted in the figure is the dispersion for a 12-period ($N_{pl}=12$) photonic lattice, where the points indicate the actual eigenfrequencies and the solid curve is a fit of the data to illustrate the case of $N_{pl}\rightarrow\infty$. The flattening of the dispersion at a band edge results in a drastic increase in the density of states. We define the density of states as $\rho(\omega)$

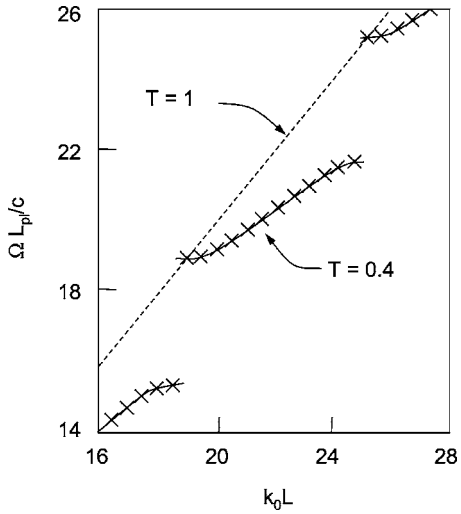

FIG. 4. Dispersion for a 12-period photonic lattice. The points are the eigenmodes, the solid curve is a fit through these points, and the dashed curve shows the free-space dispersion.

$=dk_0/d\Omega$, where following solid-state convention k_0 is the wave vector with vanishing interface reflectivity. The effects of the large density of states increase on intensity inside and outside of a photonic lattice is the focus of this paper.

III. ACTIVE MEDIUM AND RADIATION FIELD

To study the modification of emission characteristics by a photonic lattice, we consider the situation of an ensemble of two-level atoms located inside a photonic lattice. Each atom is labeled by n and j, so that $|a_{nj}\rangle$ and $|b_{nj}\rangle$ are the ground and excited states, respectively, of an atom located at z_j inside the photonic lattice, with resonant energy $\hbar\omega_n$. Assuming the dipole approximation, z_j is a parameter locating the atom to a region that is small compared to a wavelength, but large compared to the size of an atom. We describe the radiation field emitted by these atoms in terms of the combined system eigenmodes derived in the previous section—i.e.,

$$E(z,t)=\sum_k \mathcal{E}_k[a_k(t)+a_k^\dagger(t)]u_k(z), \tag{7}$$

where $\mathcal{E}_k=\sqrt{\hbar\Omega_k/(A\epsilon_0)}$, $a_k^\dagger$ and a_k are the photon creation and annihilation operators, respectively, and A is the cross section area of the structure. From Eq. (7), using Maxwell's equations and a dipole interaction, the Hamiltonian for the matter and radiation-field system is [20,21]

$$H=\sum_{n,j}\hbar\,\omega_n|b_{nj}\rangle\langle b_{nj}|+\sum_k \hbar\,\Omega_k a_k^\dagger a_k - \sum_{k,n,j} g_{kj}(|b_{nj}\rangle\langle a_{nj}|a_k+a_k^\dagger|a_{nj}\rangle\langle b_{nj}|), \tag{8}$$

where $g_{kj}=\mu\mathcal{E}_k u_k(z_j)$ and μ is the dipole matrix element. Introducing the operators for the microscopic polarization amplitude $p_{njk}\equiv|b_{nj}\rangle\langle a_{nj}|a_k\exp[-i(\omega_n-\Omega_k)t]$, the excited- and ground-state populations, $\sigma_{anj}\equiv|a_{nj}\rangle\langle a_{nj}|$ and $\sigma_{bnj}\equiv|b_{nj}\rangle\langle b_{nj}|$, respectively, and working in the Heisenberg picture [18], we derive the equations of motion

$$\frac{dp_{njk}}{dt}=\frac{i}{\hbar}e^{-i(\omega_n-\Omega_k)t}\sum_{k'} g_{k'j}(\sigma_{bnj}a_k a_{k'}^\dagger - a_{k'}^\dagger a_k\sigma_{anj}), \tag{9}$$

$$\frac{d\sigma_{anj}}{dt}=\frac{i}{\hbar}\sum_k g_{kj}[p_{njk}^\dagger e^{-i(\omega_n-\Omega_k)t}-p_{njk}e^{i(\omega_n-\Omega_k)t}], \tag{10}$$

$$\frac{d\sigma_{bnj}}{dt}=-\frac{i}{\hbar}\sum_k g_{kj}[p_{njk}^\dagger e^{-i(\omega_j-\Omega_k)t}-p_{njk}e^{i(\omega_j-\Omega_k)t}]. \tag{11}$$

Additionally, the photon number operator obeys

$$\frac{da_k^\dagger a_k}{dt}=\frac{i}{\hbar}\sum_{n,j} g_{kj}[p_{njk}^\dagger e^{-i(\omega_j-\Omega_k)t}-p_{njk}e^{i(\omega_j-\Omega_k)t}]. \tag{12}$$

Assuming that the polarization decays because of dephasing collisions and that the effective decay rate γ is much larger than the rate of changes in the active medium and photon populations, we can adiabatically eliminate the polarization

equation. Then, introducing the expectation values

$$N_k = \langle a_k^\dagger a_k \rangle, \tag{13}$$

$$N_{an} = \sum_{j=1}^{N} \langle \sigma_{anj} \rangle, \tag{14}$$

$$N_{bn} = \sum_{j=1}^{N} \langle \sigma_{bnj} \rangle, \tag{15}$$

we obtain the working equations for our analysis:

$$\frac{dN_{an}}{dt} = \frac{2\mu^2}{\hbar \epsilon_0 A L_c \gamma} \sum_k \Omega_k \Gamma_k [(N_{bn} - N_{an}) N_k + N_{bn}] L(\omega_n - \Omega_k) - \gamma_r [N_{an} - f_a(\omega_n, T)] - \Lambda(\omega_n) N_{an}, \tag{16}$$

$$\frac{dN_{bn}}{dt} = -\frac{2\mu^2}{\hbar \epsilon_0 A L_c \gamma} \sum_k \Omega_k \Gamma_k [(N_{bn} - N_{an}) N_k + N_{bn}] L(\omega_n - \Omega_k) - \gamma_r [N_{bn} - f_b(\omega_n, T)] + \Lambda(\omega_n) N_{an}, \tag{17}$$

$$\frac{dN_k}{dt} = \frac{2\mu^2}{\hbar \epsilon_0 A L_c \gamma} \sum_n \Omega_k \Gamma_k [(N_{bn} - N_{an}) N_k + N_{bn}] L(\omega_n - \Omega_k) - \gamma_c N_k, \tag{18}$$

where N is the number of atoms, $L(x) = [1 + (x/\gamma)^2]$ and

$$\Gamma_k = \int_0^{L_c} dz |u_k(z)|^2 \tag{19}$$

is the mode confinement factor. In Eqs. (16)–(18), the pump and decay contributions are included phenomenologically, γ_c is the photon decay rate, $\Lambda(\omega_n) = \Lambda_0 \exp[\hbar(\omega_0 - \omega_n)/k_B T_p]$ is the pump rate, $\hbar\omega_0$ is the material band-gap energy, and γ_r is an effective rate for the actual populations N_{an} and N_{bn} to relax to the equilibrium distributions

$$f_a(\omega_n, T) = Z_n, \tag{20}$$

$$f_b(\omega_n, T) = Z_n \exp\left(\frac{-\hbar\omega_n}{k_B T}\right), \tag{21}$$

where

$$Z_n = \left[1 + \exp\left(\frac{-\hbar\omega_n}{k_B T}\right)\right]^{-1} \tag{22}$$

and T_p and T are the pump and reservoir temperatures. In our study, Eqs. (16)–(18) are solved numerically.

IV. DETECTOR

To determine the spectra of the intracavity and output radiation, we use the simple spectrometer model shown in Fig. 5. In this model, two-level atoms are placed in the region of interest. These atoms are prepared with only the ground state $|a_n^d\rangle$ populated when the radiation field is absent (zero detector temperature). The label n indicates that the level spacing between $|b_n^d\rangle$ and $|a_n^d\rangle$ is ω_n^d. The atoms interact weakly with the radiation field to be measured, which excites some fraction of the atoms to an excited state $|b_n^d\rangle$ that has some finite lifetime γ_d^{-1}. Assuming a sufficiently fast detector response so that the detector populations adiabatically follow the variations in the photon number, the population in state $|b_n^d\rangle$ gives a measure of the radiation intensity ($\propto N_k$) in the region occupied by the detector atom. The steady-state upper-detector-state population is

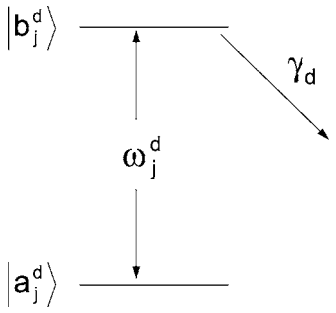

FIG. 5. Spectrometer model where the upper-level decay prevents detector saturation and approximates the drift of carriers to the electrodes in a reverse-baised photodiode.

$$N_b^d(\omega_n^d) = D \sum_k \Omega_k N_k \frac{\gamma_d}{\gamma_d^2 + (\omega_n^d - \Omega_k)^2} \int_{z_d}^{z_d + L_d} dz |u_k(z)|^2, \tag{23}$$

where $D = 2\mu_d N_d/(\hbar \epsilon_0 A L_d \gamma_d)$, μ_d is the dipole matrix element between states $|b_n^d\rangle$ and $|a_n^d\rangle$, L_d is the length of the detected region, and N_d is the number of detector atoms. Measuring this population for atoms of different ω_n^d gives the spectrum within the region $z_d \leqslant z \leqslant z_d + L_d$. In this model, N_d and the decay rate γ_b should be sufficiently large to prevent saturation of the detector. On the other hand, too large a γ_d degrades spectral resolution. Alternately, one may use two-level atoms injected into the region of interest and removed after a short time [22].

V. PHOTONIC-LATTICE EMISSION

We consider a 12-period photonic lattice with $L_c = 120$ μm, $L = 1.2$ cm, and interface transmission $T_{pl} = 0.01$, 0.1, and 0.4. The eigenmodes are determined by solving Eq. (2) with the boundary conditions (3)–(5). The results are used in Eqs. (16)–(18), which are solved numerically with a fourth-order Runge-Kutta finite-difference method. The input parameters are $\gamma = 10^{12}$ s^{-1}, $\gamma_c = 10^9$ s^{-1}, $\Lambda_0 = 10^{10}$ s^{-1}, $\omega_0 = 1.6 \times 10^{14}$ s^{-1}, $\mu = e \times 1.3$ nm, $N = 601$, and $T_p = T = 400$ K.

A. Equilibrium

To relate to earlier studies [7,10–12], we first compare photonic-lattice and blackbody emissions under thermal equilibrium conditions. To do so, we perform the calculations for a rapid population relaxation rate of $\gamma_r = 10^{13}$ s^{-1}, which ensures (verified after the time integration) that the steady-state active-medium populations N_{an} and N_{bn} are to a

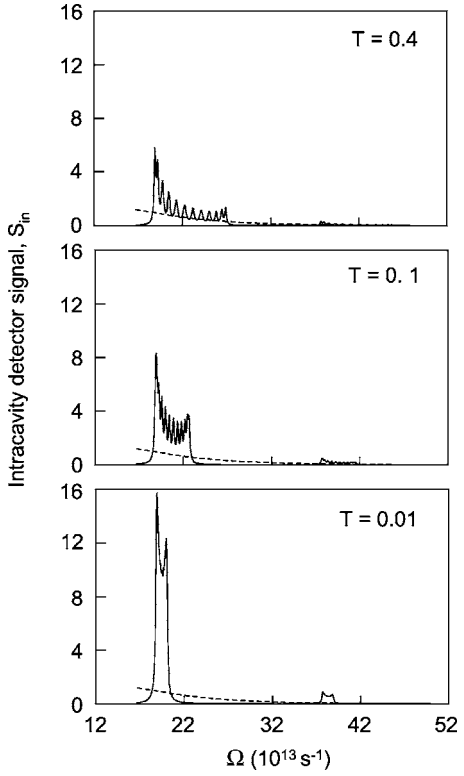

FIG. 6. Photonic-lattice (solid curves) and blackbody (dashed curves) intracavity emission spectra.

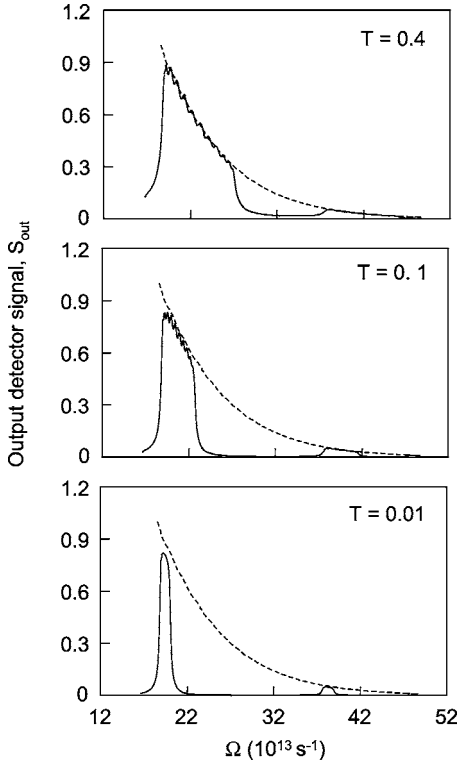

FIG. 7. Photonic-lattice (solid curves) and blackbody (dashed curves) output emission spectra.

good approximation given by the equilibrium distributions $f_a(\omega_n,T)$ and $f_b(\omega_n,T)$, respectively. The solid curves in Fig. 6 show the calculated intracavity emission spectra for three interface transmissions. In the figure, we define an intracavity detector signal

$$S_{in}(\omega) \equiv \frac{N_b^d(\omega)}{D} = \sum_k \Omega_k N_k \frac{\gamma_d}{\gamma_d^2 + (\omega - \Omega_k)^2} \int_0^{L_c} dz |u_k(z)|^2, \tag{24}$$

where $N_b^d(\omega)$ is calculated using the steady-state solution for N_k in Eq. (23). The figure shows two bands of photonic-lattice states, where the frequency extent of the bands depends on the interface transmission. Between the two bands is a photonic band gap where emission is strongly suppressed. By repeating the calculation with $T_{pl}=1$, we obtain the corresponding blackbody spectrum (dashed curve). Comparison of the curves clearly indicates the significant intensity enhancement inside a photonic lattice, especially at the band edges for $T_{pl}=0.01$.

To determine the output spectrum, we place the spectrometer in the free-space region. Figure 7 shows the output detector signal

$$S_{out}(\omega) \equiv \frac{N_b^d(\omega)}{D} = \sum_k \Omega_k N_k \frac{\gamma_d}{\gamma_d^2 + (\omega - \Omega_k)^2} \int_{L-L_c}^{L} dz |u_k(z)|^2 \tag{25}$$

for the same interface transmissions as in Fig. 6. In contrast to inside the photonic lattice, where there is significant optical intensity enhancement, Fig. 7 indicates that the intracavity emission peaks are appreciably depressed outside the photonic lattice. The strong intracavity enhancement by the photonic-lattice density of states appears to be canceled by an outcoupling attenuation. This leaves the photonic lattice emission peaks to be essentially independent of interface transmission. More importantly, these peaks lie at or slightly below the blackbody emission curve.

Simulations performed over a wide range of input parameters point towards the result that as long as the active-medium populations N_{an} and N_{bn} are in thermal equilibrium, the photonic-lattice output is always below that of the blackbody. For instance, the spectra are insensitive to the choice of γ. The blackbody spectrum is also insensitive to γ_d because of the weak frequency dependence of the blackbody photon density. However, for the photonic lattice, too large a γ_d degrades the spectrometer resolution and leads to lower spectral peaks. For the opposite situation, too small a γ_d introduces noise in the spectrum because of the inadequate resolution of the system normal modes (i.e., because L is insufficiently large).

B. Nonequilibrium

To study active photonic-lattice operation in greater generality, we allow the active-medium populations to deviate from thermal equilibrium. The investigation is performed by repeating the earlier calculations, keeping all input parameters except γ_r the same. Figure 8 illustrates the changes in the excited-state population distribution N_{bn}, at steady state and for decreasing population relaxation. When γ_r is reduced

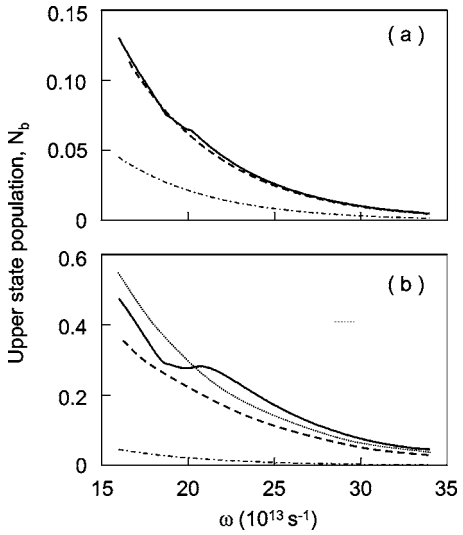

FIG. 8. Upper-state population for photonic lattice (solid curve) and blackbody (dashed curve) versus transition frequency for $\gamma_r = 10^{11}$ s (a) and 10^{10} s^{-1} (b). The dot-dashed curves show the equilibrium distribution at 400 K. The dotted curve is the equilibrium distribution at 500 K.

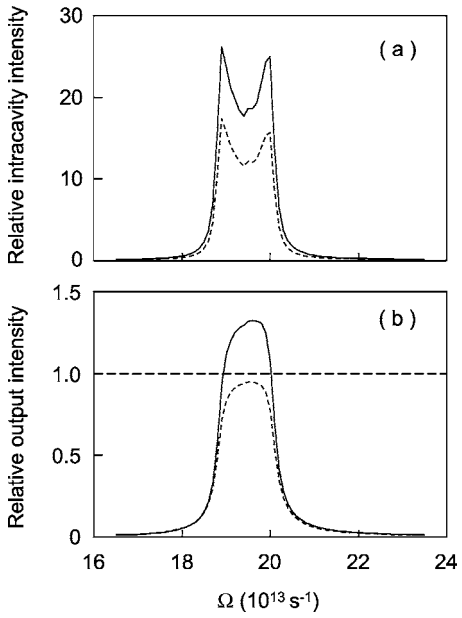

FIG. 9. Relative intensity spectra inside (a) and outside (b) the photonic lattice in Fig. 8. The curves are for $\gamma_r = 10^{11}$ s (dashed line) and 10^{10} s^{-1} (solid line). Above the long-dashed line, the photonic-lattice intensity is higher than the blackbody's.

to 10^{11} s^{-1} from 10^{13} s^{-1}, a slight difference emerges between the excited-state populations of the identically pumped photonic-lattice and blackbody active media. The solid curve in Fig. 8(a) shows a noticeable deformation of the photonic-lattice excited-state population distribution. There is also a significant difference between N_{bn} and $f_b(\omega_n, T)$ for $T = 400$ K (dot-dashed curve), which are the actual distribution and the asymptotic ($\gamma_r \to \infty$) equilibrium distribution, respectively. Further reduction to $\gamma_r = 10^{10}$ s^{-1} significantly increases the deviation of the photonic-lattice excited-state population distribution from a Maxwell-Boltzmann distribution [see solid curve, Fig. 8(b)]. Holes are burned in the distribution because the population relaxation is insufficiently fast to replenish the excited-state population depleted by the spectrally relatively narrow radiation field emitted by the photonic lattice. There is also a change in the blackbody distribution [dashed curve, Fig. 8(b)] to one that approximates a Maxwell-Boltzmann distribution at $T \approx 500$ K (dotted curve). Since the active media in both structures are identical, the difference between the photonic-lattice and blackbody populations (solid and dashed curves, respectively) is from photonic-lattice effects.

The effects of the population changes in Fig. 8 on the emission spectra are depicted in Fig. 9. Plotted on the y axis is the relative emission intensity inside (outside) the photonic lattice, which we define as $S_{in(out)}(\omega)$ for the photonic lattice divided by $S(\omega)$ for the blackbody. In spite of the large increase in excited-state population, we find that the intracavity and output relative intensities remain basically unchanged when γ_r is reduced from 10^{13} to 10^{11} s^{-1}. In particular, the output photonic-lattice intensity remains at or slightly below that of the blackbody (i.e., relative intensity $\leqslant 1$). However, the result changes considerably for $\gamma_r = 10^{10}$ s^{-1}. Here, the intensity within the photonic-lattice band increases considerably relative to that of the blackbody both inside and outside the cavity (solid curves). More importantly, the solid curve in Fig. 9(b) clearly shows greater output intensity for the photonic lattice than the blackbody throughout the emission band of the photonic lattice. This enhancement of output emission occurs for identically pumped active regions and is a result of a nonequilibrium population that shows significant hole burning. The presence of nonequilibrium effects may be the cause for experimental observations of metallic photonic-lattice emission exceeding that of the blackbody [23]. Note that the difference in output emission spectra [solid and dashed curves in Fig. 9(b)] comes from population distributions that are, on the average, quite similar. That is, a least-squares fit of the solid and dashed curves in Fig. 8(b) will produce Maxwell-Boltzmann distributions that differ in temperature by less than 20 K. Therefore, measurement of average temperature will not identify the experimental conditions leading to the photonic-lattice output emission exceeding that of the blackbody. Rather, an energy-resolved measurement of the emitter upper-state population is necessary.

The end results reached in our analyses involving equilibrium and nonequilibrium situations are robust; i.e., they are relatively insensitive to the choice of input parameters. While calculations performed with different interface transmission show significant differences in spectral shapes and intracavity intensities, the output intensities remain relatively constant because of the mitigating influence of the coupling to free space. Calculations are also performed for a different number of photonic-lattice periods. The results show negligible differences beyond $N_{pl} = 10$, thus verifying that the use of a 12-period photonic lattice does not lead to loss of generality. Clearly noticeable are effects, such as differences in excess output intensity with varying interface transmission, that are due to optical nonlinearities in the nonequilibrium active medium. Such effects will not be present in treatments using linear classical sources [12].

VI. EXTENSION TO A THREE-DIMENSIONAL PHOTONIC LATTICE

This section treats a three-dimensional photonic lattice. Following earlier quantum optical studies of photonics lattices [24], a spherically symmetric dielectric function is assumed to simplify the numerics. In spherical coordinates, the equation satisfied by the passive eigenmodes of the combined photonic-lattice and free-space system, $u_{klm}(r,\theta,\phi)$, is

$$\frac{1}{r}\frac{\partial^2}{\partial r^2}(ru_{klm}) + \frac{1}{r^2\sin\theta}\frac{\partial}{\partial\theta}\left(\sin\theta\frac{\partial u_{klm}}{\partial\theta}\right) + \frac{1}{r^2\sin^2\theta}\frac{\partial^2 u_{klm}}{\partial\phi^2} = -\mu_0\epsilon(r)\Omega_{klm}^2 u_{klm}. \quad (26)$$

Choosing the dielectric function

$$\epsilon(r) = \epsilon_0\left[1 + \frac{\eta}{\bar{k}}\sum_{j=1}^{N_{pl}}\delta(r-r_j)\right], \quad (27)$$

where η and $\bar{k}$ are the same as in Eq. (1), a solution of Eq. (26) between the photonic-lattice interfaces or in the free-space region is

$$u_{klm}(r,\theta,\phi) = [A_{kln}\, j_l(kr) + B_{kln}\,\eta_l(kr)]Y_{lm}(\theta,\phi), \quad (28)$$

where $j_l(\rho)$ and $\eta_l(\rho)$ are spherical Bessel and Neumann functions, $Y_{lm}(\theta,\phi)$ is a spherical harmonic, and the subscript n indicates that the coefficients A_{kln} and B_{kln} are for $r_n < r \leqslant r_{n+1}$. In order for a solution to be finite at the origin and vanish at $r = r_{N_{pl}+1}$ (the end of the region representing free space), we require

$$B_{kl1} = 0, \quad (29)$$

$$A_{klN_{pl}+1} j_l(kr) + B_{klN_{pl}+1}\,\eta_l(kr) = 0. \quad (30)$$

At the interfaces, the boundary conditions (4) and (5) demand

$$A_{kln}\, j_l(kr) + B_{kln}\,\eta_l(kr) - A_{kln+1} j_l(kr) - B_{kln+1}\,\eta_l(kr) = 0, \quad (31)$$

$$A_{kln}[-j_l'(kr) + \eta j_l(kr)] + B_{kln}[-\eta_l'(kr) + \eta\eta_l(kr)] + A_{kln+1} j_l'(kr) + B_{kln+1}\,\eta_l'(kr) = 0, \quad (32)$$

for $2 \leqslant n \leqslant N_{pl}$ and $r = r_1, r_2, \ldots, r_{N_{pl}}$.

The numerical solution is implemented similar to what is described in the Appendix. A six-period photonic lattice is considered, where the lattice constant is 2 μm and the interface transmission is $T_{pl}=0.05$. Coupled to the photonic lattice is a "free"-space region extending from 24 μm $< r \leqslant 612$ μm. The system dynamics is governed by the equations of motion (16)–(18) with the photon-state index k replaced by the three indices k, l, and m. Numerical analyses of the steady-state solutions are performed assuming the input parameters $\gamma = 2\times10^{12}$ s^{-1}, $\gamma_r = 10^{13}$ s^{-1}, $\gamma_c = 10^{12}$ s^{-1}, $\Lambda_0 = 10^{12}$ s^{-1}, $\omega_0 = 1.6\times10^{14}$ s^{-1}, $\mu = e\times 1.3$ nm, $N=601$, and $T_p = T = 200$ K. Similar to the one-dimensional case, the rates are chosen to ensure reaching steady state with active-medium populations N_{an} and N_{bn} described by Maxwell-Boltmann distributions.

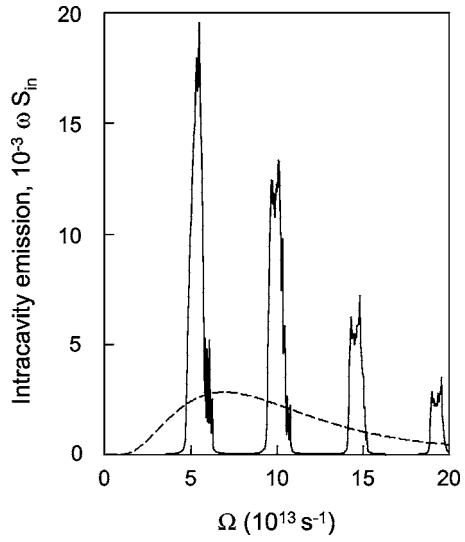

FIG. 10. Intracavity three-dimensional photonic-lattice and blackbody emission spectra (solid and dashed curves, respectively).

To obtain the intracavity emission spectrum, detector atoms are placed inside the photonic-lattice structure. The probability of finding a photon with frequency ω is proportional to

$$S_{in}(\omega) = \sum_{klm}\Omega_{klm}N_{klm}\frac{\gamma_d}{\gamma_d^2 + (\omega-\Omega_{klm})^2} \times \int_0^{2\pi} d\phi \int_0^{\pi} d\theta \int_0^{r_{Npl}} dr\, r^2 |u_{klm}(r,\theta,\phi)|^2, \quad (33)$$

so that the emission energy is proportional to $\hbar\omega S_{in}(\omega)$. In Fig. 10, the solid curve is a plot of ωS_{in} as a function of frequency. It shows four narrow emission bands separated by photonic band gaps. Repeating the calculation using interface transmission $T_{pl}=1$ gives the free-space emission spectrum (dashed curve). Examination of the populations after steady state is reached verifies that both solid and dashed curves are for identical Maxwell-Boltmann distributions at $T=200$ K. The curves clearly indicate intensity enhancement inside the photonic lattice.

To compare the output emission in a given direction, the detector atoms are placed to give a signal

$$S_{out}(\omega) = \sum_{klm}\Omega_{klm}N_{klm}\frac{\gamma_d}{\gamma_d^2 + (\omega-\Omega_{klm})^2} \times \int_{\phi_{d1}}^{\phi_{d2}} d\phi \int_{\theta_{d1}}^{\theta_{d2}} d\theta \int_{rd1}^{r_{d2}} dr\, r^2 |u_{klm}(r,\theta,\phi)|^2,$$

where r_{d1} and r_{d2} are within the free-space region, θ_{d1}, θ_{d2} and ϕ_{d1}, ϕ_{d2} define the direction and collection solid angles. The solid curve and dashed curves in Fig. 11 show the output photon-lattice and free-space emission spectra, respectively. These results are obtained for $r_{d1}=100$ μm, $r_{d2}=124$ μm, $\phi_{d1}=\theta_{d1}=0$, $\phi_{d2}=2\pi$, and $\theta_{d2}=\pi/18$, which define emission within a cone of $\pm10^\circ$ in the z direction. Comparison of solid and dashed curves indicates that, similar to the one-

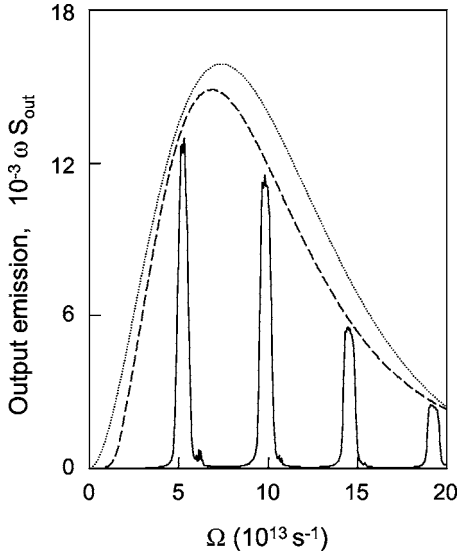

FIG. 11. Output emission spectra for 3D photonic-lattice (solid curve), blackbody (dashed curve), and Planck's (dotted curve) distributions.

dimensional case, peak intensities measured outside the photonic-lattice structure do not exceed those of the blackbody.

A test of our treatment is to see how well it reproduces Planck's distribution for the frequency spectrum of free-space emission energy from a thermal source. The dotted curve in Fig. 11 is proportional to $\omega^3[\exp(\hbar\omega/k_BT)-1]^{-1}$ with temperature $T=200$ K, and it depicts the shape of the blackbody frequency spectrum according to Planck's formula. The agreement is good, considering that there are several factors causing discrepancies. Two important ones are truncating the optical modes at $l=13$ and limiting "free"-space to $24\ \mu\text{m} < r \leqslant 612\ \mu\text{m}$, in order to maintain reasonable computation times. Even so, over 10^4 optical modes are used. Other factors contributing to the differences include the presence of optical loss [$\gamma_c \neq 0$ in Eq. (18)], which is neglected in the derivation of Planck's distribution. While increasing the number of optical modes improves agreement with Planck's formula, it does not impact the blackbody versus photonic-lattice emission comparison. This is because the result of the photonic-lattice output intensity spectrum being bounded inside the blackbody one applies separately for each l.

VII. CONCLUSION

In summary, the emission from an active photonic lattice is investigated using a model consisting of an inhomogeneously broadened ensemble of two-level atoms interacting with a multimode radiation field. A fully quantized (i.e., quantized atoms and quantized electromagnetic field) description is chosen to provide a consistent description of stimulated and spontaneous emission. Furthermore, to describe the modal properties of the radiation field of a finite photonic lattice coupled to free space, the analysis considers the photonic lattice and free space as one combined system. This circumvents a long-standing inconsistency in quantum optics involving the decoupling of the treatments of the cavity normal modes and outcoupling losses.

Our approach gives the emission spectra for arbitrary photonic-lattice configurations and reproduces Planck's blackbody radiation formula for thermal emission in free space. Comparison of photonic-lattice and blackbody emission shows appreciable modification of the blackbody spectrum by the photonic lattice, where the redistribution of the photon density of states results in a suppression of radiation at certain wavelengths and enhancement at others. The enhancement can give rise to high-intracavity-intensity peaks, especially at the photonic-lattice band edges. These intensity peaks are mitigated outside the photonic lattice by the spectrally dependent outcoupling. For population relaxation sufficiently fast to ensure the same equilibrium population distribution in both structures, the photonic-lattice output intensity does not exceed that of the blackbody at the same frequency. However, for slow population relaxation, there is a greater tendency for a nonequilibrium photonic-lattice population. Then, in the presence of population hole burning, the intensity in certain regions of the photonic-lattice spectrum can exceed that of the blackbody, even when both structures are identically pumped.

ACKNOWLEDGMENTS

This work was supported by the U.S. Department of Energy under Contract No. DE-AC04-94AL85000 and by the Alexander von Humboldt Foundation. The author thanks I. El-Kady, I. Waldmueller and S. Wieczorek for helpful discussions.

APPENDIX: NUMERICAL EVALUATION OF SYSTEM EIGENMODES

In this appendix we describe a numerical procedure for evaluating the eigenmodes of the combined photonic-lattice and free-space system. This procedure applies for a photonic lattice of arbitrary size and interface transmission. In region n, which may be any section of the photonic lattice or the section representing free space, the solutions of Eq. (2) have the form

$$u_k(z_n) = A_{k,n}\sin(kz_n) + B_{k,n}\cos(kz_n), \tag{A1}$$

where $k=\Omega_k/c$. Because of boundary condition (3),

$$A_{k,1} \neq 0, \tag{A2}$$

$$B_{k,1} = 0, \tag{A3}$$

$$A_{k,N_{pl}+1}\sin(kz_{N_{pl}+1}) + B_{k,N_{pl}+1}\cos(kz_{N_{pl}+1}) = 0. \tag{A4}$$

From boundary conditions (4) and (5),

$$A_{k,n}\sin(kz_n) + B_{k,n}\cos(kz_n) = A_{k,n+1}\sin(kz_n) + B_{k,n+1}\cos(kz_n), \tag{A5}$$

$$A_{k,n}[-\cos(kz_n)+\eta\sin(kz_n)]+B_{k,n}[\sin(kz_n)+\eta\cos(kz_n)] = -A_{k,n+1}\cos(kz_n)+B_{k,n+1}\sin(kz_n), \quad \text{(A6)}$$

for $2\leqslant n\leqslant N_{pl}$.

There are many approaches to numerically solve the above equations. We describe below the one we followed in this paper. Basically, we look for values of k satisfying Eq. (A4), where the mode amplitudes $A_{k,N_{pl}+1}$ and $B_{k,N_{pl}+1}$ are obtained by solving a $2N_{pl}\times 2N_{pl}$ matrix equation

$$SU = D. \quad \text{(A7)}$$

The matrix elements of S are best defined by separating the even- and odd-number rows. For $n=$odd,

$$S_{i,i} = -\sin(kz_1), \quad \text{(A8)}$$

$$S_{i,i+1} = -\cos(kz_i), \quad \text{(A9)}$$

and for $n=$even,

$$S_{i,i} = -\sin(kz_{i-1}). \quad \text{(A10)}$$

For $n\geqslant 3$ and $n=$odd,

$$S_{i,i-1} = \cos(kz_i), \quad \text{(A11)}$$

$$S_{i,i-2} = \sin(kz_i), \quad \text{(A12)}$$

and for $n\geqslant 4$ and $n=$even,

$$S_{i,i-1} = \cos(kz_{i-1}), \quad \text{(A13)}$$

$$S_{i,i-2} = \sin(kz_{i-1})+\eta\cos(kz_{i-1}), \quad \text{(A14)}$$

$$S_{i,i-3} = -\cos(kz_{i-1})+\eta\sin(kz_{i-1}). \quad \text{(A15)}$$

All other matrix elements are zero. The elements of the column matrix D vanish except for

$$D_1 = -\sin(kz_1), \quad \text{(A16)}$$

$$D_2 = \cos(kz_2)-\eta\sin(kz_2). \quad \text{(A17)}$$

Equation (A7) is solved using the Gauss-Jordan method. In the solutions and for $j=$odd, U_j gives the coefficient $A_{k,j+1}$, while U_{j+1} gives the coefficient $B_{k,j+1}$. At this stage, we have set $A_{k,1}=1$ so that the eigenfunctions are unnormalized. We perform the normalization according to Eq. (6).

[1] E. Yablonovitch, Phys. Rev. Lett. **58**, 2059 (1987).
[2] S. John, Phys. Rev. Lett. **58**, 2486 (1987).
[3] P. Pigeat, D. Rouxel, and B. Weber, Phys. Rev. B **57**, 9293 (1998).
[4] S.-Y. Lin, J. G. Fleming, E. Chow, J. Bur, K. K. Choi, and A. Goldberg, Phys. Rev. B **62**, R2243 (2000).
[5] J. G. Fleming, S. Y. Lin, I. El-Kady, R. Biswas, and K. M. Ho, Nature (London) **417**, 52 (2002).
[6] Z.-Y. Li, Phys. Rev. B **66**, 241103(R) (2002).
[7] C. M. Cornelius and J. P. Dowling, Phys. Rev. A **59**, 4736 (1999).
[8] S.-Y. Lin, J. Moreno, and J. G. Fleming, Appl. Phys. Lett. **83**, 380 (2003).
[9] S.-Y. Lin, J. G. Fleming, and I. El-Kady, Opt. Lett. **28**, 1909 (2003).
[10] A. Narayanaswamy and G. Chen, Phys. Rev. B **70**, 125101 (2004).
[11] T. Trupke, P. Würfel, and M. A. Green, Appl. Phys. Lett. **84**, 1997 (2004).
[12] C. Luo, A. Narayanaswamy, G. Chen, and J. D. Joannopoulos, Phys. Rev. Lett. **93**, 213905 (2004).
[13] For a textbook discussion see A. E. Siegman, *Lasers* (University Science Books, Mill Valley, CA, 1986), Chap. 24.
[14] W. E. Lamb, Jr., Phys. Rev. **134**, A1429 (1964).
[15] R. Lang, M. O. Scully, and W. E. Lamb, Jr., Phys. Rev. A **7**, 1788 (1973).
[16] A. Narayanaswamy and G. Chen, Phys. Rev. B **70**, 125101 (2004).
[17] For a recent discussion, see D. Kleppner, Phys. Today **58**(2), 30 (2005).
[18] W. H. Louisell, *Quantum Statistical Properties of Radiation* (Wiley, New York, 1973).
[19] M. B. Spencer and W. E. Lamb, Jr., Phys. Rev. A **5**, 884 (1972).
[20] M. O. Scully and M. S. Zubairy, *Quantum Optics* (Cambridge University Press, Cambridge, England, 1977).
[21] N. Vats, S. John, and K. Busch, Phys. Rev. A **65**, 043808 (2002).
[22] M. O. Scully and W. E. Lamb, Jr., Phys. Rev. **166**, 246 (1968).
[23] S.-Y. Lin, J. Moreno, and J. G. Fleming, Appl. Phys. Lett. **84**, 1999 (2004).
[24] S. John and J. Wang, Phys. Rev. B **43**, 12772 (1991).